

Deep Recurrent Disease Progression Model for Conversion-Time Prediction of Alzheimer’s Disease

Wonsik Jung^a, Eunji Jun^a, Heung-Il Suk^{a,b,*},
and the Alzheimer’s Disease Neuroimaging Initiative¹

^a*Department of Brain and Cognitive Engineering, Korea University, Seoul 02841, Republic of Korea*

^b*Department of Artificial Intelligence, Korea University, Seoul 02841, Republic of Korea*

Abstract

Alzheimer’s disease (AD) is known as one of the major causes of dementia and is characterized by slow progression over several years, with no treatments or available medicines. In this regard, there have been efforts to identify the risk of developing AD in its earliest time. While many of the previous works considered cross-sectional analysis, more recent studies have focused on the diagnosis and prognosis of AD with longitudinal or time series data in a way of disease progression modeling (DPM). Under the same problem settings, in this work, we propose a novel computational framework that forecasts the phenotypic measurements of MRI biomarkers and predicts the clinical statuses at multiple future time points. However, in handling time series data, it generally faces with many unexpected missing observations. In regard to such an unfavorable situation, we define a secondary problem of estimating those missing values and tackle it in a systematic way by taking account of temporal and multivariate relations inherent in time series data. Concretely, we propose a deep recurrent network that jointly tackles the three problems of (i) missing value imputation, (ii) phenotypic measurements forecasting, and (iii) clinical status prediction of a subject based on his/her longitudinal imaging biomarkers. Notably, the learnable model parameters of our network are trained in an end-to-end manner with our circumspectly defined loss function. In our experiments over The Alzheimer’s Disease Prediction Of Longitudinal Evolution (TADPOLE) challenge cohort, we measured performance for various metrics and compared our method to competing methods in the literature. Exhaustive analyses and ablation studies were also conducted to better confirm the effectiveness of our method.

Keywords: Disease Progression Modeling, Alzheimer’s Disease, Deep Learning, Recurrent Neural Networks, Missing Value Imputation, Longitudinal Data, Mild Cognitive Impairment, Conversion-Time Prediction

*Corresponding author: Heung-Il Suk (hisuk@korea.ac.kr)

¹Data used in preparation of this article were obtained from the Alzheimer’s Disease Neuroimaging Initiative (ADNI) database (<http://www.loni.ucla.edu/ADNI>). As such, the investigators within the ADNI contributed to the design and implementation of ADNI and/or provided data but did not participate in analysis or writing of this report. A complete listing of ADNI investigators can be found at http://adni.loni.ucla.edu/wpcontent/uploads/how_to_apply/ADNI_Authorship_List.pdf.

1. Introduction

Alzheimer's disease (AD) is a catastrophic and progressive neurodegenerative disease that is clinically characterized by the impairment of cognitive and functional abilities along with behavioral symptoms. It is known that AD is the most common cause of dementia, accounting for about 70% of age-related dementia (Alzheimer's Association, 2019). It is estimated that there are approximately 50 million AD patients around the world, and the figure will double by 2030 (Patterson, 2018), thus causing great social and economic burdens (Brookmeyer et al., 2007; Alzheimer's Association, 2019). Unfortunately, there is currently no pharmaceutical or clinical treatment available to reverse or cure the progression of AD (Marinescu et al., 2018; Gaugler et al., 2019). When considering the characteristics of patients with AD, the clinical symptoms that disturb the activities of daily living, such as memory loss, language impediment, and other malfunctions, become apparent only after several years from the time that the brain is initially affected by the disease (Braak and Braak, 1996; Morris et al., 1996). For this reason, it is of great importance to identify the emergence of the disease at its earliest stage or predict the risk of emergence as early as possible.

In recent decades, leveraging the advances in machine learning, especially deep learning, there have been efforts to formulate the task of neuroimaging-based early AD diagnosis or prognosis as regression and classification problems (Zhang et al., 2011; Suk et al., 2014, 2016; Liu et al., 2018b). On the one hand, many of the existing studies focused on cross-sectional data analysis for AD diagnosis (Suk and Shen, 2013; Cheng et al., 2017; Liu et al., 2018a). These studies showed reasonable performance in the clinical status prediction task, even though only baseline features were used. However, they have limitations that did not properly model the progressive deterioration of the disease and different occurrence time for each individual, which are characteristics of AD.

On the other hand, in order to better utilize the available historical data, *i.e.*, longitudinal data, disease progression modeling (DPM) has drawn researchers' attention (Sukkar et al., 2012; Peterson et al., 2017; Lee et al., 2019; Lorenzi et al., 2019), especially for prediction of the time-to-conversion to the next clinical status in the AD spectrum. The AD progression generally involves not only the acceleration of regional volume atrophy (*e.g.*, the hippocampus, which is presumed to show the earliest morphological changes due to AD) but also increased enlargement of the ventricle over time (Nestor et al., 2008). These types of changes can be better captured from longitudinal data, which allows for learning the underlying temporal characteristics in the disease. Thus, with DPM, it may be possible to forecast the future changes in phenotypic measurements and predict the time of conversion in clinical statuses that are symptomatically categorized as cognitively normal (CN), mild cognitive impairment (MCI), and dementia (Mills and Tamnes, 2014). In particular, a better understanding of the individual disease progression contributes to more accurate diagnosis, monitoring, and prognosis, which are respectively beneficial for early diagnosis, intervention, and personalized care (Oxtoby and Alexander, 2017). In this work, we focus on neuroimaging-based DPM for AD prognosis and time-to-conversion prediction in the AD spectrum.

For the DPM, conversion time prediction is critical, as it gives us meaningful information about the dis-

ease progression and the severity of the disease. It is much more challenging than just predicting whether the patient will progress to AD. Conversion time prediction in this study is analogous to survival analysis (Miller Jr, 2011; Oulhaj et al., 2009; Thung et al., 2018). Survival analysis is the study of time-to-event data, modeling the expected period until event occurrence (*e.g.*, disease status conversion) at a future time. Although conversion time prediction resembles survival analysis, they actually tackle different approaches. First, survival analysis focuses on predicting the probability of AD conversion at different future time points. However, conversion time prediction forecasts when the conversion of the disease will occur. For example, in general, probability methods (*e.g.*, Cox regression model) are used to access the survival problems, while conversion time prediction is based on typical regression methods (*e.g.*, least-squares regression model) (Thung et al., 2018). Our work investigates both problems.

In the literature on survival analysis and related fields, DPM has been widely applied when the causes of diseases were not well-known or various factors were involved. Although working with longitudinal data is useful for improving our knowledge of the disease, adding a temporal dimension entails different forms of difficulties in data analysis, such as increasing dimensionality, missing values, and time alignment problems (Ibrahim and Molenberghs, 2009). In a longitudinal dataset, there could be samples of subjects with one or two follow-ups ('short-term') and those of subjects with a large number of follow-ups ('long-term') after the first visit. With short-term data, we might not suffer from missing measurements and data imbalance problems, but we are restricted from learning patterns of long-range dependence by nature, thus limited in building a reliable model for DPM (Ardekani et al., 2017; Fiot et al., 2014; Gray et al., 2012; Shi et al., 2017). Meanwhile, long-term longitudinal data are potentially better suited for DPM by allowing us to get better insights into the global patterns in disease progression (Bilgel et al., 2015; Guerrero et al., 2016; Bilgel et al., 2016; Aghili et al., 2018), but generally have issues of many missing measurements and time alignment, due to research or patients drop out or unexpected accidents, *etc.* (Petersen et al., 2010).

Some studies (Wei et al., 2016; Zhang et al., 2012; Misra et al., 2009) have been developed for MCI-to-AD conversion, which represents who will progress to AD. (Wei et al., 2016) used MRI thickness measures as features to predict MCI-to-AD conversion. They used data at the baseline and up to 18 months (short-term samples). Meanwhile, (Misra et al., 2009) used longitudinal MRI data to extract the changes of brain atrophy for detecting MCI-to-AD conversion. However, this study employed a short period follow-up data (up to 15 months). In addition, Zhang *et al.* also utilized longitudinal MRI data up to 24 months to predict clinical scores as well as the conversion of MCI patients by longitudinal feature selection method that extracts the brain regions across multiple time points (Zhang et al., 2012).

More recently, we have witnessed the potential of deep learning methods (Wang et al., 2018; Lee et al., 2019; Ghazi et al., 2019; Jung et al., 2019) for DPM thanks to their favorable characteristics of learning feature representations from data, rather than engineering feature manually. Especially, recurrent neural networks (RNNs) and their variants have been mostly employed because of their methodological ability to handle the time alignment issue among intra- and inter-subject trajectories. In particular, long short-term memory

(LSTM) (Hochreiter and Schmidhuber, 1997) is one of the successful techniques to encode temporal patterns (Wang et al., 2018; Yoon et al., 2018; Ghazi et al., 2019; Jung et al., 2019) by capturing long-term dependencies among multivariate measurements over time with efficient gating-based operations (Gers et al., 1999; Gers and Schmidhuber, 2001). However, its use in DPM remains challenging with incomplete samples, *i.e.*, missing measurements in the data. For that reason, the previous works (Lipton et al., 2016; Wang et al., 2018; Ghazi et al., 2019; Yoon et al., 2018) have mostly involved the step of missing value imputation either as a means of preprocessing prior to training RNNs (Lipton et al., 2016; Wang et al., 2018) or by regarding it as a sub-task of the target model training for prediction (Yoon et al., 2018).

For example, Lipton *et al.* exploited RNNs with LSTM cells to diagnose the pediatric intensive care unit (PICU) from clinical time series data (Lipton et al., 2016). Wang *et al.* also used them to predict future clinical scores given 11 yearly observations (Wang et al., 2018). When training their method, all missing values of the patients' historical observations due to varying number of visits and uneven time intervals, were first imputed by simple mean or forward imputation methods (Lipton et al., 2016; Wang et al., 2018), disregarding both the temporal relations and multivariate relations of observations. Ghazi *et al.* formulated the task of AD progression modeling by means of predicting changes in volumetric MRI biomarkers in a vanilla LSTM with peephole connections (Gers and Schmidhuber, 2000) added to all the gates (Ghazi et al., 2019). In their work, when training their model, all the missing values of longitudinal samples were initialized with zeros, and no further imputation update was conducted. Here, we named this model as PLSTM-Z. It is also noteworthy that for the clinical status prognosis, they built a separate classifier with linear discriminant analysis (LDA) by taking the predicted biomarker values from the trained PLSTM-Z as input features.

Since the performance of predictive models with preprocessing-based missing value imputation are highly dependent on the static values, *e.g.*, zeros and means, determined manually or statistically, some researchers have devoted their efforts to constructing adaptive and dynamic imputation models. For example, Yoon *et al.* focused on the task of missing value imputation and utilized a bi-directional RNN to better take into account temporal relations, but no relations among multivariate features, for mortality prediction with electronic health records (Yoon et al., 2018). More recently, Cao *et al.* gave special attention to the task of missing values imputation in time series data (Cao et al., 2018). In particular, given a sequence of observations in a fixed time interval, they designed the LSTM model, the one in the original time order and the other in the reversed time order, to maximally utilize the inherent temporal relations along with multivariate relations. However, due to the use of a time-reversed sequence, their imputation method is not applicable for disease progression modeling, which is what we care about for long-term prognosis.

Inspired by the recent work of dynamic imputation methods described above, in this work, we hypothesize that both multivariate and temporal relations inherent in longitudinal data could be informative to estimate missing values. It is also believed that the appropriately imputed values help enhance the predictive power of a model for downstream tasks, *i.e.*, in our work, volumetric MRI biomarker changes and clinical status prognosis over multiple time points ahead, thus making it possible to infer time-to-conversion in the AD spectrum.

In these regards, we propose a unified framework that can (i) adaptively impute missing values ('*imputation module*'), (ii) encode imputed observations into latent representations via LSTM ('*encoding module*'), and (iii) predict both future MRI volumetric measurements and clinical statuses ('*prediction module*') over time in terms of the AD progression from a subject's historical measurements. Methodologically, we devise an imputation architecture that takes advantage of the encoded latent representations from an LSTM cell, *i.e.*, temporal relations, and utilizes multivariate relations among variables to infer missing values. For the temporal encoding in LSTM-Z (LSTM with zero imputation), we feed the *complete* observation, *i.e.*, replace the missing values with imputed ones, a mask vector that indicates which values are imputed, and the information of time-delay from the last observed times. These all together greatly help to better encode and capture temporal characteristics in a longitudinal sample for modeling disease progression. Further, we also design an objective function such that the network parameters of all the three modules can be trained jointly in an end-to-end manner.

We evaluated the performance of our proposed method using the longitudinal cohorts from 'The Alzheimer's Disease Prediction Of Longitudinal Evolution (TADPOLE)' Challenge² in terms of (i) future volumetric biomarker regression and (ii) clinical status classification, respectively. Furthermore, we conducted exhaustive analyses to verify the effectiveness of the proposed framework for AD progression in three aspects, namely, model perspective analysis, longitudinal stability analysis, and personalized analysis.

The main contributions of our work can be summarized as follows:

- To the best of our knowledge, our work is the first to use a novel deep recurrent network that jointly performs missing value imputation, future MRI biomarker forecasting, and clinical status prognosis over multiple time points in a unified framework.
- A multi-objective function for the proposed imputation-encoding-prediction network is devised and optimized in an end-to-end manner.
- Compared to the competing methods considered in our experiments, our proposed method outperformed them in all metrics for imputation, regression, and classification.

This work extends the preliminary version published by (Jung et al., 2019) by revising the network architecture and performing more rigorous experiments and analyses.

2. Materials and Preprocessing

In this work, we used the TADPOLE longitudinal cohort³ from the ADNI database, including ADNI-1, ADNI-2, and ADNI-GO. The main objective of the challenge was to track the progression of subjects with AD using MRI biomarkers and clinical measurements. The dataset includes 1,500 kinds of longitudinal MRI

²<https://tadpole.grand-challenge.org/>

³Available at '<https://tadpole.grand-challenge.org/Data/>'

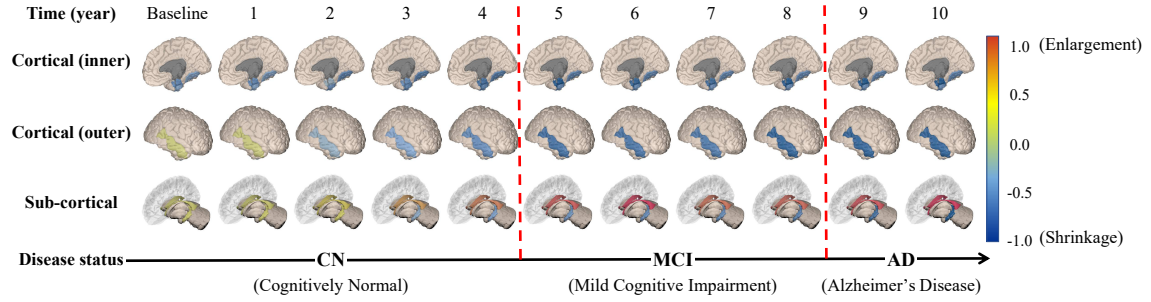
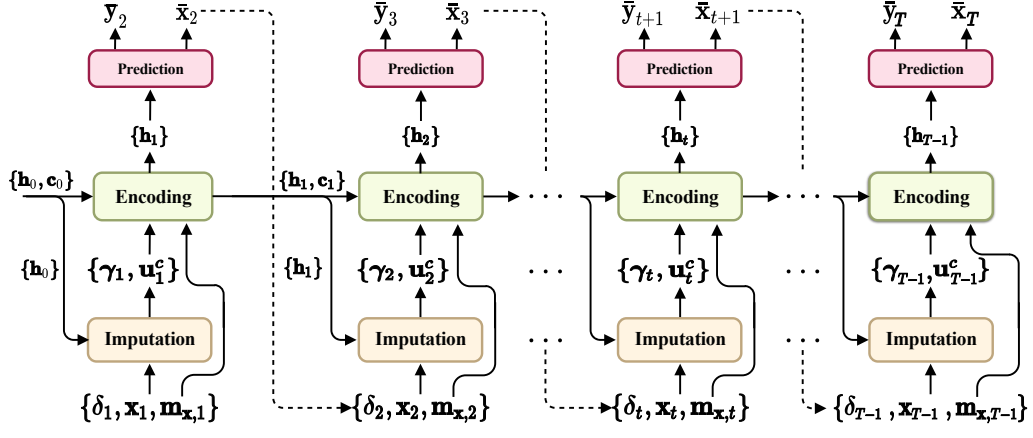


Figure 1: An example of morphological changes of six regions in a subject’s brain. The color-coded values indicate the amount of volume changes from a baseline time point. The darker color of either blue or red, the more shrunk or enlarged volume from a baseline time point.

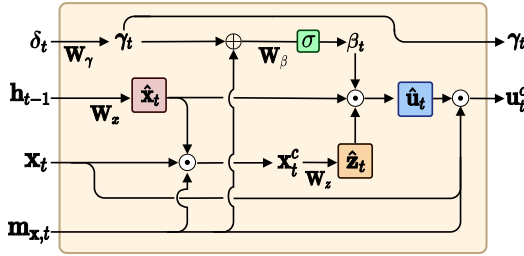
biomarkers, *e.g.*, cortical thickness and cortical volume, from 1,737 patients (aged from 54.40 up to 91.40) with 12,741 visits at 22 different time points between 2003 and 2017 (Marinescu et al., 2018). The summary of the TADPOLE dataset is presented in Table A.1.

As our main objective in this work is to predict the yearly progression, we considered 11 regular visits out of 22 total visits. In the TADPOLE dataset, the clinical groups were labeled as 342 AD, 417 CN, 310 EMCI (early MCI), 562 LMCI (late MCI), and 106 SMC (significant memory concern). Like the previous work (Ghazi et al., 2019; Jung et al., 2019), we merged the groups of CN and SMC into CN, and EMCI and LMCI into MCI, thus resulting in three categories: CN, MCI, and AD. Moreover, from the original TADPOLE dataset, we excluded subjects with no visit on the baseline or having less than 3 visits, resulting in a total of 773 subjects in the end. The number of longitudinal measurements ranges from 4 to 11 with $5.76(\text{mean}) \pm 2.07(\text{std})$. The duration of sequences ranges from 36 to 120 with $61.54(\text{mean}) \pm 27.21(\text{std})$. The detailed information of demographic and clinical scores for samples used in our work is summarized in Table C.2 over 11 yearly time points. Note that there are many missing observations in the MRI biomarkers and clinical labels over the selected dataset.

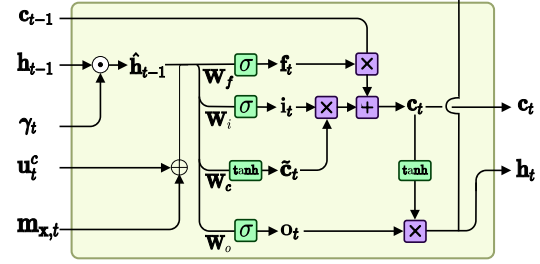
Although the TADPOLE dataset offers numerous kinds of biomarkers to forecast the AD status (Marinescu et al., 2018), by following (Ghazi et al., 2019) in this paper, we considered the six volumes of ventricles, hippocampus, fusiform gyrus, middle temporal gyrus, entorhinal cortex, and whole-brain, extracted from the T1-weighted MRI that are shown in Fig. B.1. We normalized the original values of the biomarkers with each subject’s intracranial volume (ICV) to compensate for the inter-subject variability in brain size (Davis and Wright, 1977; Ghazi et al., 2019) and further conducted feature-wise linear normalization based on the min/max values to be in the range of $[-1, 1]$. For a reference, we illustrated an example of morphological changes of six regions in a subject’s brain, who experienced three clinical statuses during the 11-year period, in Fig. 1.



(a) A proposed deep recurrent network architecture



(b) An architecture of our imputation module



(c) An architecture of our encoding module

Figure 2: (a) The architecture of the proposed method combines three modules, *i.e.*, imputation, encoding, and prediction. The modules impute the missing values of the current input, forecast the biomarker values, and predict the clinical status at the next time sequence. (b) Operations to consider the feature-based relations and temporal relations in estimating missing values. (c) A variant of a vanilla LSTM unit with γ and $\mathbf{m}_{\mathbf{x},t}$. For simplicity, the biases are excluded. If unobserved, the predicted values are used as the input of the next time step, which is denoted as dotted arrows. Solid arrows indicate the process of architecture.

3. Proposed Method

In this work, we propose a novel framework for AD progression modeling with incomplete longitudinal data. Specifically, our proposed method is composed of three modules, namely, an imputation module, encoding module, and prediction module, as illustrated in Fig. 2a. At a certain time point, the imputation module first estimates missing values using the encoded latent representations from the previous time point in a deep recurrent network, as well as the multivariate relations among the observed values of the current time point. Second, the encoding module receives the *complete* observation with the missing values replaced by imputed ones, a mask vector that indicates which values are imputed, and the information of time-delay from the last observed time points. They encode and capture temporal characteristics in the given longitudinal data. Lastly, the encoded representations are transformed to forecast the volumetric measurements and predict the clinical status of the next time point.

3.1. Notations

Throughout the paper, we denote matrices as boldface uppercase letters, vectors as boldface lowercase letters, and scalars as normal italic letters. For a matrix \mathbf{A} , its (i, j) -th element and the i -th column are denoted as $A(i, j)$ and \mathbf{a}_i , respectively. For a vector \mathbf{a} , its i -th element is denoted as $a(i)$.

Assume that a set of multivariate time series of D variables over T times from N number of subjects are given $\{\mathbf{X}^{(n)}, \mathbf{Y}^{(n)}\}_{n=1}^N$, where $\mathbf{X}^{(n)} = [\mathbf{x}_1^{(n)}, \dots, \mathbf{x}_t^{(n)}, \dots, \mathbf{x}_T^{(n)}] \in \mathbb{R}^{D \times T}$, $\mathbf{Y}^{(n)} = [\mathbf{y}_1^{(n)}, \dots, \mathbf{y}_t^{(n)}, \dots, \mathbf{y}_T^{(n)}] \in \{0, 1\}^{K \times T}$, and K denotes the number of classes considered in a target task. In our case, it corresponds to the clinical state of a patient, *i.e.*, CN, MCI, and AD. To limit clutter, hereafter we omit the superscript (n) unless it is unclear in the context.

To better use the temporal information regarding both missing value imputation and latent feature representation, we will consider a time delay for each observation from the last observation time. For this, we define an auxiliary variable $\mathbf{s} \in \mathbb{R}^T$ that indicates when the observations were acquired, and a time delay matrix $\Delta \in \mathbb{R}^{D \times T}$, whose elements *i.e.*, $\Delta(d, t)$ or δ_t , are set as follows:

$$\Delta(d, t) = \begin{cases} \mathbf{s}(t) - \mathbf{s}(t-1) + \Delta(d, t-1) & \text{if } t > 1, M_{\mathbf{x}}(d, t-1) = 0, \\ \mathbf{s}(t) - \mathbf{s}(t-1) & \text{if } t > 1, M_{\mathbf{x}}(d, t-1) = 1, \\ 1 & \text{if } t = 1. \end{cases}$$

3.2. Missing Values Imputation

We design an architecture that jointly exploits temporal and multivariate relations for imputation. Our imputation module is based on a deep recurrent neural network, which becomes an encoding module as described in Section 3.3. Specifically, we take the hidden state values of a recurrent network for the context of temporal relations in a given sequence.

At time t , the previous temporal context information up to $(t-1)$ is encoded in the hidden state \mathbf{h}_{t-1} of an encoding module. From the hidden state \mathbf{h}_{t-1} , we first use the temporal relations for the estimation of the MRI measurements of the current time t as follows:

$$\hat{\mathbf{x}}_t = \mathbf{W}_x \mathbf{h}_{t-1} + \mathbf{b}_x \quad (1)$$

where \mathbf{W}_x and \mathbf{b}_x are learnable parameters. Then, by exploiting the masking vector $\mathbf{m}_{\mathbf{x}, t}$, we obtain a temporary vector \mathbf{x}_t^c by replacing the missing values with those estimated from the temporal relations, while maintaining the observed MR features as follows:

$$\mathbf{x}_t^c = \mathbf{m}_{\mathbf{x}, t} \odot \mathbf{x}_t + (\mathbf{1} - \mathbf{m}_{\mathbf{x}, t}) \odot \hat{\mathbf{x}}_t. \quad (2)$$

We also consider multivariate relations among the MRI features of the imputed temporal vector \mathbf{x}_t^c in Eq. (2) by introducing learnable parameters \mathbf{W}_z and \mathbf{b}_z as follows:

$$\hat{\mathbf{z}}_t = \mathbf{W}_z \mathbf{x}_t^c + \mathbf{b}_z. \quad (3)$$

Here, it should be noted that we constrain the diagonal elements in \mathbf{W}_z to be zero, such that the values of elements in $\hat{\mathbf{z}}_t$ are obtained from those of the other variables in \mathbf{x}_t^c only, thereby focusing purely on the multivariate relations.

Using temporal and multivariate relations, two imputed vectors, \mathbf{x}_t^c and $\hat{\mathbf{z}}_t$, are obtained as described above. Now, for robustness, we further consider combining these two vectors by introducing a weighting coefficient vector that is dynamically determined, based on the missing patterns. Regarding the missing patterns, there are two sources of information, the masking vector $\mathbf{m}_{\mathbf{x},t}$ and the time delay from the last observation in δ_t . We use the time delay information by defining a time decay factor $\gamma_t \in (\mathbf{0}, \mathbf{1}]^D$ as follows:

$$\gamma_t = \exp\{-\max(\mathbf{0}, \mathbf{W}_\gamma \delta_t + \mathbf{b}_\gamma)\} \quad (4)$$

where \mathbf{W}_γ and \mathbf{b}_γ are tunable parameters. Combining this time decay factor with a masking vector via concatenation, we compute the weighting coefficient vector β_t as follows:

$$\beta_t = \sigma(\mathbf{W}_\beta \cdot [\gamma_t \oplus \mathbf{m}_{\mathbf{x},t}] + \mathbf{b}_\beta) \quad (5)$$

where σ denotes a logistic sigmoid function to guarantee that the coefficients are in the range of $(0, 1)$. Thus, β_t carries the integrated information about the time decay factors γ_t and the missing patterns at the current time step. With this weighting coefficient vector β_t , we finally estimate the missing values using an interpolation between $\hat{\mathbf{x}}_t$ and $\hat{\mathbf{z}}_t$

$$\hat{\mathbf{u}}_t = \beta_t \odot \hat{\mathbf{z}}_t + (1 - \beta_t) \odot \hat{\mathbf{x}}_t. \quad (6)$$

Consequently, we obtain the ‘*complete*’ observation vector \mathbf{u}_t^c by replacing the missing values with the estimates in Eq. (6)

$$\mathbf{u}_t^c = \mathbf{m}_{\mathbf{x},t} \odot \mathbf{x}_t + (1 - \mathbf{m}_{\mathbf{x},t}) \odot \hat{\mathbf{u}}_t. \quad (7)$$

3.3. Recurrent Temporal Encoding and Multi-task Prediction

After imputing the missing values, we exploit deep recurrent network for temporal encoding. Here, to better reflect the existence of missing values in an observation, we devise a novel computational mechanism, *i.e.*, a variant of a vanilla LSTM cell with γ and $\mathbf{m}_{\mathbf{x},t}$. In other words, the complete value \mathbf{u}_t^c in Eq. (7) is fed into the recurrent model.

First, as in the imputation module, we use the time delay information in δ_t , which is one of the important sources for temporal patterns (Che et al., 2018). That is, although the temporal context information up to the previous time ($t - 1$) is represented in the hidden state \mathbf{h}_{t-1} of a recurrent network, their influence in encoding with the current observation \mathbf{u}_t^c should be treated in different ways depending on when the ‘real’ last observation was acquired. Therefore, we use this crucial information with a temporal decaying factor γ_t in Eq. (4) before embedding with the current observation \mathbf{u}_t^c as follows:

$$\hat{\mathbf{h}}_{t-1} = \mathbf{h}_{t-1} \odot \gamma_t. \quad (8)$$

Meanwhile, we also feed the masking vector $\mathbf{m}_{\mathbf{x},t}$ to the encoding module to let it know which values are the imputed ones estimated from our imputation module. Concretely, the internal operations in our encoding module are as follows:

$$\begin{aligned}
\mathbf{f}_t &= \sigma \left(\mathbf{W}_f \cdot [\hat{\mathbf{h}}_{t-1}, \mathbf{u}_t^c \oplus \mathbf{m}_{\mathbf{x},t}] + \mathbf{b}_f \right) \\
\mathbf{i}_t &= \sigma \left(\mathbf{W}_i \cdot [\hat{\mathbf{h}}_{t-1}, \mathbf{u}_t^c \oplus \mathbf{m}_{\mathbf{x},t}] + \mathbf{b}_i \right) \\
\tilde{\mathbf{c}}_t &= \tanh \left(\mathbf{W}_c \cdot [\hat{\mathbf{h}}_{t-1}, \mathbf{u}_t^c \oplus \mathbf{m}_{\mathbf{x},t}] + \mathbf{b}_c \right) \\
\mathbf{c}_t &= \mathbf{f}_t \cdot \mathbf{c}_{t-1} + \mathbf{i}_t \cdot \tilde{\mathbf{c}}_t \\
\mathbf{o}_t &= \sigma \left(\mathbf{W}_o \cdot [\hat{\mathbf{h}}_{t-1}, \mathbf{u}_t^c \oplus \mathbf{m}_{\mathbf{x},t}] + \mathbf{b}_o \right) \\
\mathbf{h}_t &= \mathbf{o}_t \cdot \tanh(\mathbf{c}_t)
\end{aligned}$$

where $\{\mathbf{W}_f, \mathbf{W}_i, \mathbf{W}_c, \mathbf{W}_o, \mathbf{b}_f, \mathbf{b}_i, \mathbf{b}_c, \mathbf{b}_o\}$ are the learnable parameters of our modified LSTM cell. $\mathbf{f}_t, \mathbf{i}_t, \tilde{\mathbf{c}}_t$, and \mathbf{o}_t represent the outputs of the forget, input, update, output gates, respectively.

Based on the hidden state representation \mathbf{h}_t from the encoding module, our prediction module produces two outcomes, *i.e.*, the MRI measurements $\bar{\mathbf{x}}_{t+1}$ and the clinical state $\bar{\mathbf{y}}_{t+1}$ of the next time point. We use simple linear and logistic regression models for each of the outcomes as follows:

$$\bar{\mathbf{x}}_{t+1} = \mathbf{W}_g \mathbf{h}_t + \mathbf{b}_g \quad (9)$$

$$\bar{\mathbf{y}}_{t+1} = \text{softmax}(\mathbf{W}_y \mathbf{h}_t + \mathbf{b}_y) \quad (10)$$

where $\mathbf{W}_g, \mathbf{W}_y, \mathbf{b}_g$, and \mathbf{b}_y are parameters. Thus, our prediction module is connected with the encoding module, and the parameters can be tuned jointly with those of the encoding module. From a learning stand-point, this prediction module takes the advantage of a multi-task learning strategy for more predictive representations, comparable to the work of (Ghazi et al., 2019), where they first conducted MRI measurements forecasting and then built an independent classifier for clinical status prediction. In Section 5.1, we present the validity of our multi-task learning by comparing it with the counterpart single-task learning.

3.4. Learning

We defined a composite loss function for the joint training of the three modules, *i.e.*, missing value imputation, temporal encoding, and output prediction. Specifically, for the imputation loss $\mathcal{L}_{\text{imputation}}$, we measure the similarity between the observed data and the imputed data by the mean absolute error (MAE) from three different perspectives, *i.e.*, temporal relations in Eq. (1), multivariate relations in Eq. (3), and composite relations in Eq. (6).

$$\mathcal{L}_{\text{imputation}} = \sum_{t=1}^T (|\tilde{\mathbf{x}}_t - \hat{\mathbf{x}}_t| + |\tilde{\mathbf{x}}_t - \hat{\mathbf{z}}_t| + |\tilde{\mathbf{x}}_t - \hat{\mathbf{u}}_t|) \odot (1 - \tilde{\mathbf{m}}_{\mathbf{x},t}) \quad (11)$$

where $\tilde{\mathbf{x}}_t = \mathbf{x}_t \odot \mathbf{m}_{\mathbf{x},t}$ and $\tilde{\mathbf{M}}_{\mathbf{x},t}$ is a masking matrix of random removal from observations for imputation module training only. Empirically, when comparing with a loss defined only with the final imputed values $\mathbf{u}_{\mathbf{x}}^c$ in Eq. (7), *i.e.*, $|\tilde{\mathbf{x}}_t - \mathbf{u}_{\mathbf{x}}^c|$, the joint loss in Eq. (11) enhanced the stability and speed in training.

As for the MRI biomarker prediction loss $\mathcal{L}_{\text{biomarkers}}$, we assessed the correspondence between the model prediction $\bar{\mathbf{x}}_{t+1}$ and the future real MRI measurements \mathbf{x}_{t+1} as follows:

$$\mathcal{L}_{\text{biomarkers}} = \sum_{t=1}^{T-1} (\mathbf{x}_{t+1} \odot \mathbf{m}_{\mathbf{x},t+1} - \bar{\mathbf{x}}_{t+1} \odot \mathbf{m}_{\mathbf{x},t+1})^2. \quad (12)$$

Lastly, for the clinical prognosis, we exploited the focal cross-entropy loss $\mathcal{L}_{\text{prognosis}}$ (Lin et al., 2017) due to the imbalance in samples among the class labels:

$$\mathcal{L}_{\text{prognosis}} = - \sum_{t=1}^{T-1} \mathbf{m}_{\mathbf{y},t} \left[\sum_{k=1}^K \mathbf{y}_t(k) (1 - \bar{\mathbf{y}}_t(k))^\epsilon \log(\bar{\mathbf{y}}_t(k)) \right] \quad (13)$$

where ϵ is a hyperparameter ($\epsilon \geq 0$). Therefore, we define the overall loss function $\mathcal{L}_{\text{total}}$ as follows:

$$\mathcal{L}_{\text{total}} = \alpha \mathcal{L}_{\text{imputation}} + \zeta \mathcal{L}_{\text{biomarkers}} + \xi \mathcal{L}_{\text{prognosis}} \quad (14)$$

where α , ζ , and ξ are the hyperparameters to weight the corresponding losses. The optimization of this loss function allows us to train all the parameters of the three modules, *i.e.*, imputation, encoding, and prediction, via stochastic gradient descent in an end-to-end manner.

4. Experimental Results and Analysis

4.1. Experimental Settings

We validated the effectiveness of the proposed framework that systematically unifies data-driven missing value imputation and multi-task learning for AD progression modeling in tasks of missing value imputation at the current time and MRI biomarker forecasting and clinical status prediction, we made predictions for every time point (with a one-year interval between consecutive time points) up to 11 time points, thus the next 10 years from the baseline. For each time point, the prediction was conducted based on all the observed historical values and the predicted or imputed values, if unobserved or missing.

We reported the average test results from 5-fold cross-validation. Specifically, we partitioned the dataset described in Section 2 into three non-duplicated subsets for training, validation, and testing. For rigorous evaluation, we randomly selected 10% of the subjects in each class as the validation set and another 10% as the test set from the baseline time point. For the imputation task, we randomly removed 10% of the ‘true’ observation values in samples from all train, validation, and test sets and then used them as the ground truth. However, we utilized all true observation values for the prediction tasks. For quantitative evaluation, we used the metrics of MAE and mean relative error (MRE) for the imputation task, MAE for the MRI biomarker prediction task, and multi-class area under the receiver operating characteristic curve (mAUC) (Hand and Till, 2001) for the clinical status prediction task. We also conducted statistical significance tests in comparison with the competing methods. Briefly, we used the paired, two-sided Wilcoxon signed-rank test (Wilcoxon, 1992) for regression tasks, *i.e.*, imputation and MRI biomarkers forecast, on MAE and MRE. Meanwhile, McNemar’s test (McNemar, 1947) on mAUC was applied for the clinical status prediction task.

Table 1: Performance for an imputation task in terms of MAE and MRE (mean \pm std). The best performance is indicated in boldface.

Models	MAE	MRE
LSTM-M (Wang et al., 2018)	$0.076 \pm 0.014^\dagger$	$0.260 \pm 0.063^\dagger$
LSTM-F (Lipton et al., 2016)	$0.073 \pm 0.012^\dagger$	$0.246 \pm 0.045^\dagger$
MRNN (Yoon et al., 2018)	$0.145 \pm 0.022^*$	$0.485 \pm 0.102^*$
PLSTM-Z (Ghazi et al., 2019)	$0.107 \pm 0.013^*$	$0.376 \pm 0.052^*$
Ours	0.073 ± 0.009	0.239 ± 0.056

(* : $p < 0.05$, \dagger : no statistical difference)

We compared our proposed method with the following methods that deal with missing values imputation and prediction tasks:

- Mean imputation with LSTM (LSTM-M) (Wang et al., 2018): Missing values were imputed with the mean values of the respective variables in a training set, and a standard LSTM network was used for temporal encoding and MRI biomarker prediction, which was then used for classification with LDA.
- Forward imputation with LSTM (LSTM-F) (Lipton et al., 2016): This is the same as the LSTM-M, except that the missing values were imputed with the most recent observed values.
- Zero imputation with Peephole LSTM (PLSTM-Z) (Ghazi et al., 2019): A peephole LSTM (Gers and Schmidhuber, 2000) was used for MRI biomarker prediction with missing values imputed by zeros as input. The predicted MRI biomarkers were then used for classification via LDA.
- Multi-directional RNN (MRNN) (Yoon et al., 2018): This operates forward and backward within the intra-stream directions, *i.e.*, for each variable, and in the inter-stream directions, *i.e.*, among variables. Unlike a typical bidirectional-RNN, the timing of inputs into the hidden layers was lagged in the forward direction and advanced in the backward direction. The network outputted the MRI biomarker measures for the next time point, which were then fed into LDA for clinical status prediction.

For all the competing methods, we set 64 hidden units and trained them using an Adam optimizer (Kingma and Ba, 2014) with a learning rate of 5×10^{-3} , a mini-batch size of 64, and an epoch of 300. To avoid an overfitting problem and make the training curve converge considerably, we applied an ℓ_2 -regularization by setting the corresponding coefficient to 10^{-4} . Regarding the hyperparameters of the composite loss function in Eq. (14), we set them as $\alpha = 1.0$, $\zeta = 1.0$, and $\xi = 0.75$. In Eq. (13), we set $\epsilon = 4$. For evaluation on the test set, we chose the optimal parameters of the comparative networks that achieved the highest mAUC over the validation set.

Table 2: Performance of forecasting MRI biomarkers one-year later in terms of MAE (mean \pm std). The smallest MAE for each MRI biomarker is highlighted in boldface.

Models	MAE ($\times 10^{-3}$)					
	Ventricles	Hippocampus	Whole Brain	Entorhinal Cortex	Fusiform Gyrus	Middle Temporal Gyrus
LSTM-M (Wang et al., 2018)	$8.47 \pm 1.81^*$	$0.40 \pm 0.05^*$	$30.04 \pm 7.50^*$	$0.30 \pm 0.05^*$	$0.89 \pm 0.22^*$	$0.97 \pm 0.19^*$
LSTM-F (Lipton et al., 2016)	$8.93 \pm 2.50^*$	$0.42 \pm 0.02^*$	$28.96 \pm 7.36^*$	$0.27 \pm 0.05^{\dagger}$	$0.90 \pm 0.09^*$	$0.97 \pm 0.17^*$
MRNN (Yoon et al., 2018)	$5.02 \pm 0.84^*$	$0.33 \pm 0.03^*$	$21.07 \pm 2.26^*$	$0.26 \pm 0.02^*$	$0.70 \pm 0.05^*$	$0.80 \pm 0.07^*$
PLSTM-Z (Ghazi et al., 2019)	$2.79 \pm 0.44^{\dagger}$	$0.29 \pm 0.08^{\dagger}$	$16.75 \pm 4.59^{\dagger}$	$0.23 \pm 0.04^*$	$0.56 \pm 0.08^{\dagger}$	$0.64 \pm 0.09^{\dagger}$
Ours	2.21 ± 1.42	0.18 ± 0.04	11.82 ± 2.31	0.19 ± 0.02	0.42 ± 0.08	0.51 ± 0.09

(* : $p < 0.05$, \dagger : no statistical difference)

4.2. Performances

4.2.1. Missing Value Imputation

We presented the experimental results of the missing values imputation in Table 1. First, it is noteworthy that our proposed method achieved the lowest MAE and MRE scores, outperforming all the competing methods under our consideration with a statistical significance of $p < 0.05$ for MRNN and PLSTM-Z, but not for LSTM-M and LSTM-F. Interestingly, LSTM-M and LSTM-F, which took the simple mean or the last observed values for imputation, achieved relatively better performance than their counterpart method of PLSTM-Z that imputed with zeros and applied a peephole LSTM. Further, as for the MRNN, even though it used the multi-directional information of temporal and multivariate relations, it reported the highest MAE and MRE scores. Although both our proposed method and MRNN utilized two kinds of information sources, *i.e.*, temporal relations and multivariate relations, our method further considered missing patterns in \mathbf{M}_x and time delay in Δ systematically through a series of operations, as described in Section 3.2. We believe that this systematic imputation significantly enhanced the performance. The related more rigorous ablation study on the effectiveness of the time delay and missing pattern information is presented in Section 5.2.

4.2.2. MRI Biomarkers Forecast

The forecast errors in MAE over six MRI biomarkers are presented in Table 2. Unlike the imputation task, LSTM-M and LSTM-F, which used simple imputation, and typical LSTM resulted in relatively higher errors across the MRI biomarkers. Meanwhile, the use of temporal and multivariate relations for hidden state representation in MRNN helped to boost performance compared to LSTM-M and LSTM-F. From those results, it could be hypothesized that the MRI biomarker forecast was not necessarily helpful to the downstream task. However, our understanding of this phenomenon is that because the amount of longitudinal changes of the MRI biomarker values had been small, the simple static values were somehow close to the ground truth on

Table 3: Performance on a multi-class (AD vs. MCI vs. CN) classification task (mean \pm std). The best performance in each metric is highlighted in boldface.

Models	mAUC	Recall	Precision
LSTM-M (Wang et al., 2018)	0.688 \pm 0.048***	0.607 \pm 0.209	0.492 \pm 0.077
LSTM-F (Lipton et al., 2016)	0.659 \pm 0.108***	0.475 \pm 0.193	0.480 \pm 0.060
MRNN (Yoon et al., 2018)	0.724 \pm 0.015*	0.635 \pm 0.166	0.489 \pm 0.086
PLSTM-Z (Ghazi et al., 2019)	0.712 \pm 0.007***	0.624 \pm 0.148	0.480 \pm 0.110
Ours	0.750\pm0.030	0.655\pm0.228	0.501\pm0.085

(* : $p < 0.05$, ** : $p < 0.01$, *** : $p < 0.001$, †: no statistical difference)

average, but it was not helpful for those simple static values to capture the temporal and multivariate relations inherent in the data. As for PLSTM-Z, whose major difference from LSTM-M, LSTM-F, and MRNN was the use of a peephole LSTM, it achieved much better MAE scores for all the biomarkers. However, our proposed method⁴ was even superior to PLSTM-Z, with margins of 0.58 (ventricles), 0.11 (hippocampus), 4.93 (whole brain), 0.04 (entorhinal cortex), 0.14 (fusiform gyrus), and 0.13 (middle temporal gyrus). From those results, we argue that the piece of masking pattern information played a key roles, as discussed in Section 5.2.

4.2.3. Clinical Status Prediction

In the clinical status prediction task, due to high imbalance in sample sizes among the three classes of AD, MCI, and CN, we also reported precision and recall, along with mAUC, in Table 3. Notably, like the MRI biomarker forecast, LSTM-M and LSTM-F based on the standard LSTM architecture were inferior to the other competing methods. Among the comparative methods, MRNN (Yoon et al., 2018) resulted in boosted performance in all metrics of mAUC, recall, and precision. Meanwhile, our proposed method⁵ outperformed all the competing methods by achieving the highest scores in mAUC, recall, and precision with margins of 0.026, 0.020, and 0.012, respectively, compared to MRNN.

5. Discussion

5.1. Effect of Multi-task Learning

It is noteworthy that in the clinical status prediction task, one of the major differences of our method from the other comparative methods was to jointly optimize the parameters of the MRI biomarker forecast regressor and the clinical status prediction classifier. Thus, we also conducted an experiment by modifying our method such that it was trained with a single task of MRI biomarker prediction, and then independently

⁴The yearly detailed performance of our method is presented in Table D.3.

⁵The yearly computed performance of our method and the respective confusion matrices are presented in Table D.3 and Fig. D.2, respectively.

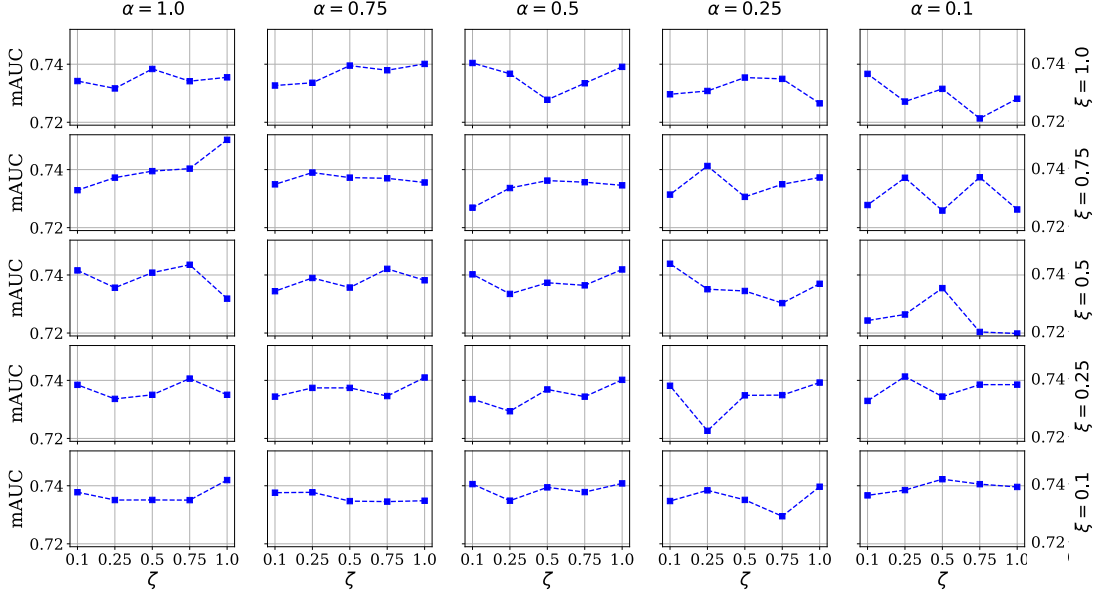


Figure 3: Result of ablation studies regarding the influence of a pair of hyper-parameters in the loss function $\{\alpha, \zeta, \xi\}$ in the classification task on the TADPOLE dataset.

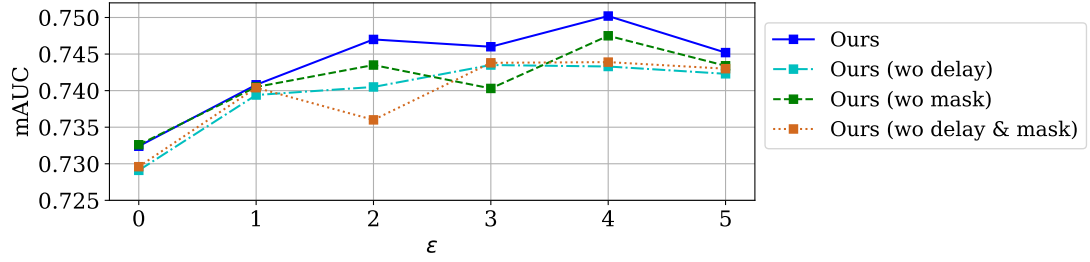


Figure 4: Result of ablation studies on the effectiveness of the time delay and missingness information for the proposed method. In this case, we selected the classification results from the setting of the ϵ value, which is the hyperparameter in the focal loss function.

trained an LDA-based classifier, under the same condition as the comparative models. That is, we trained our model by setting the hyperparameters of $\xi = 0$ ($\alpha = 1.0, \zeta = 1.0$) in the composite loss function.

In single-task learning, the results of our method were 0.734 ± 0.015 in mAUC, 0.558 ± 0.159 in recall, and 0.478 ± 0.114 in precision, respectively, which are still higher than the counterpart methods with a margin of 0.046 (vs. LSTM-M), 0.075 (vs. LSTM-F), 0.010 (vs. MRNN), and 0.022 (vs. PLSTM-Z) in terms of mAUC. When comparing between single-task and multi-task learning in our proposed method, the joint learning of MRI biomarker forecast and clinical status prediction was helpful at enhancing the performance by 0.016 in mAUC, 0.097 in recall, and 0.023 in precision.

5.2. Ablation Studies

As a part of the ablation study, we first investigated the effect of varying the pair $\{\alpha, \zeta, \xi\}$ as the hyperparameters, which is introduced in Eq. (14). We considered these parameters as a ratio to weigh the missing

values and future biomarker regression and clinical status classification to achieve optimal performance. For each parameter, we defined a set of range values for these hyperparameters as $\{0.1, 0.25, 0.5, 0.75, 1.0\}$, illustrated in Fig. 3. Derived from the highest validation AUC, our proposed method reached the highest average AUC score of 0.750 with $\alpha = 1.0$, $\zeta = 1.0$, and $\xi = 0.75$.

Unlike the comparative methods in our experiments, our proposed method used a focal loss that considers the imbalance of samples among classes. Thus, we experimented by varying the value of the hyperparameter ϵ in Eq. (13) from 0 to 5 with an interval of 1. The result is presented in Fig. 4 with a blue solid line. Note that when $\epsilon = 0$, which corresponds to the conventional cross-entropy loss, the mAUC was 0.732 ± 0.020 still outperforming the competing methods. Clearly, due to the high imbalance in the number of samples in our training set, it was useful in improving the performance to apply non-zero values for ϵ , recording the highest when $\epsilon = 4$.

To justify the effect of using the missingness information, *i.e.*, the use of mask vectors, and the time-delay information between observed values, we also conducted experiments with and without those pieces of information. The results are shown in Fig. 4. Although there were no consistent patterns in the effect of delay and missingness information, it is worth mentioning that their joint use always achieved the highest performance over different values of ϵ .

5.3. Prediction at Multiple Time Points within a 10-Year Range

To verify the validity of our proposed method for multiple-time-points prediction, we compared the prognostic performance between MRNN, PLSTM-Z, and our method, which ranked in the top three in mAUCs for single next-time-point prediction in Table 3. At each time point, we made clinical status predictions for multiple subsequent time points up to 10 years beyond the baseline with the historical observations and the imputed or predicted values for missing ones. To do this, we divided 10 cases based on the number of historical time points used for clinical status prediction, and then measured the mAUC for each case. As an example, for case 5, when having used 5 historical time points, from 0 (baseline) to 4 (4 years), then the clinical statuses over the following 5 time points (5 years) were predicted, along with the MRI biomarker forecast. The mAUC of those methods over time are presented with line graphs in Fig. 5. In the figure, we also plotted our proposed method's performance in one-time-point prediction with a dotted blue line for reference. First, from a bias-variance point of view, our proposed method notably showed high (*i.e.*, low-bias) and stable (*i.e.*, low-variance) mAUC scores across the cases. Meanwhile, PLSTM-Z and MRNN showed low mAUC (*i.e.*, high-bias) and unstable mAUC (*i.e.*, high-variance), respectively. Second, the data-driven imputation methods of MRNN and ours were superior to the counterpart method of PLSTM-Z.

For the early identification of the risk for a subject who is possibly to progress to AD, we also considered the predictive accuracy of our method in terms of conversion-to-AD within the period of consideration. Based on our 10-year range prognosis, we measured the accuracy and MAE for the conversion-to-AD, and the results are illustrated in Fig. 6. In the figure, we observed that the accuracies improved, and MAE decreased, across the cases.

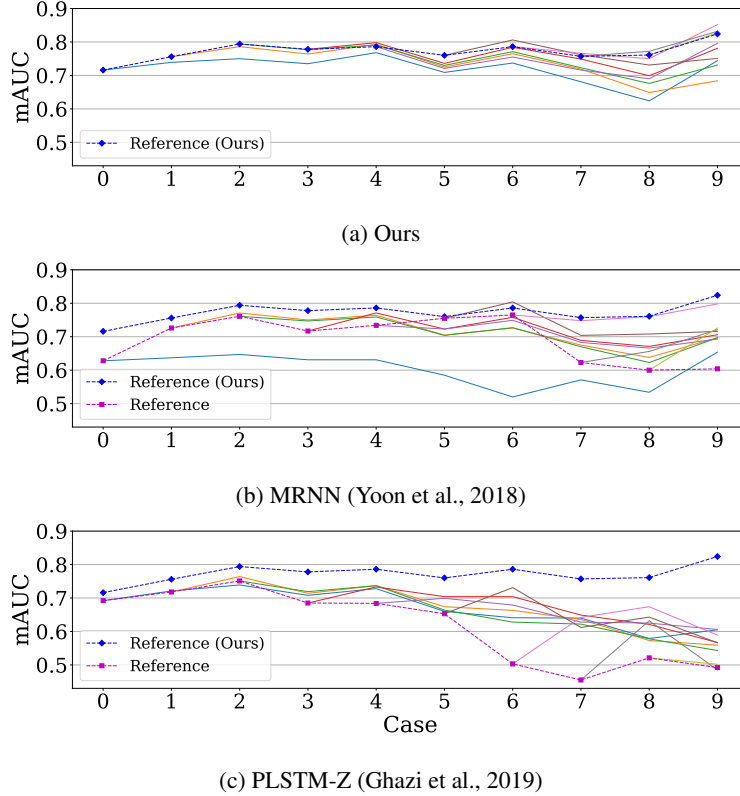


Figure 5: Disease prognostic results from historical observations between the proposed method, MRNN, and PLSTM-Z. From top to bottom, the panels display the disease prognostic performance over time using our method, MRNN, and PLSTM-Z. Specifically, the colored lines in each panel mean that the patient’s disease prognosis results are represented using accumulated data up to that point. In addition, we plotted the comparative method’s performance in one-time-point prediction with a dotted magenta line.

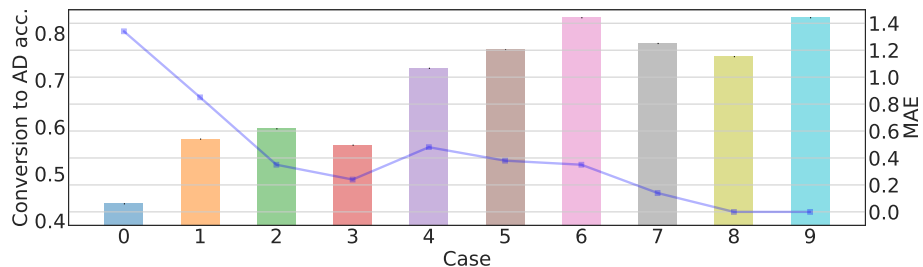


Figure 6: Conversion-to-AD accuracy for our proposed method. Each box indicates the ability to capture changes in a patient’s disease status. Furthermore, the solid line represents the absolute values of the difference between the actual patient label transition time and the model’s predictive label conversion time. Note that each case denotes that conversion-to-AD predictions are performed using data accumulated up to that time.

5.4. Irreversible Neurodegenerative Alzheimer’s Disease

The predictive models should also reflect such pathological characteristics as the irreversible neurodegeneration of AD. That is, if a subject is under the state of AD at one point, it is not expected for the subject to reverse to MCI or CN in the future. With this consideration, we compared the longitudinal clinical status

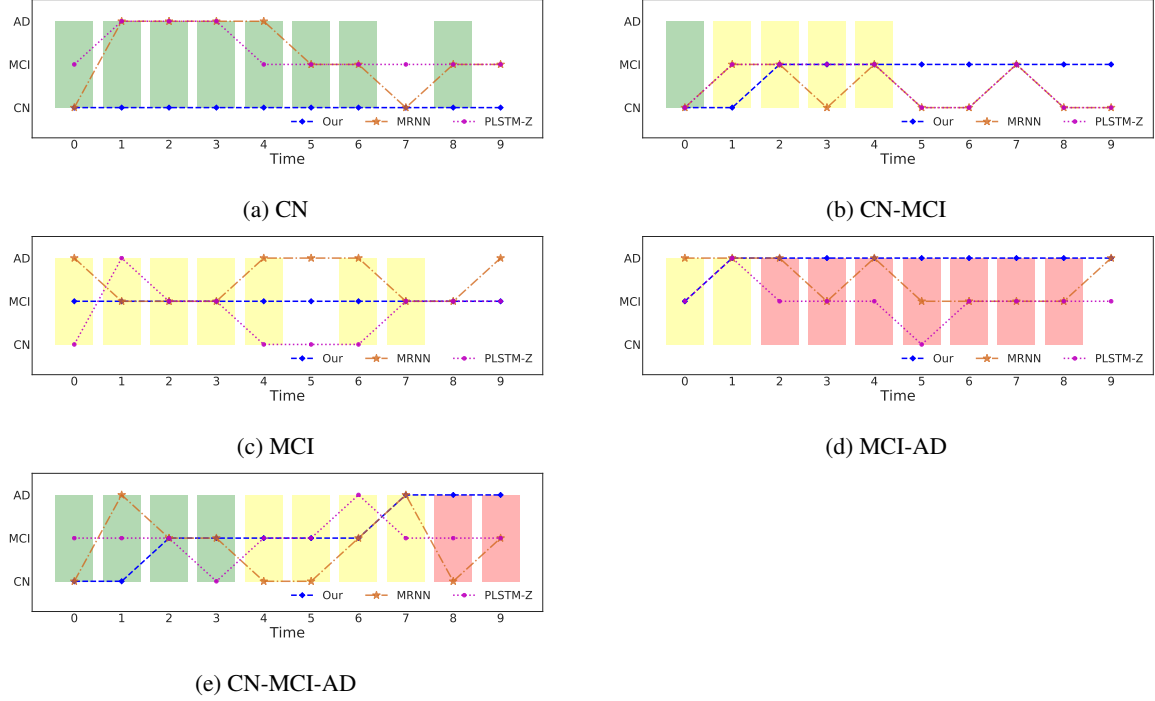


Figure 7: Results of longitudinal status prediction between the proposed method, MRNN, and PLSTM-Z. The plots in each panel represent clinical status conversion from different subjects. Green, yellow, and red represent CN, MCI, and AD in the true label, respectively.

predictions of MRNN, PLSTM-Z, and our proposed method, shown in Fig. 7. In the figure, we presented predictions for five different subjects with different progression types. While MRNN and PLSTM-Z made many state-reversing predictions, our proposed method did not show any such non-acceptable predictions. For the subjects with CN (Fig. 7a) or MCI (Fig. 7c), our method predicted CN or MCI over the whole period. In Fig. 7b, 7d, and 7e, although predictions are misplaced ahead or behind by one or two time points, our method did not make any state-reversing predictions.

5.5. Interpreting Cell States

While our deep recurrent network achieved relatively superior performance in both MRI biomarker forecasting and clinical status prediction, it is desirable to understand the dynamics of the internal state representations of our proposed model. In this regard, we devised a novel analysis method of the cell states in our LSTM. To determine which cell states contributed to the identification of the clinical statuses, we estimated the correlation between a patient’s disease statuses over time and the corresponding cell state representations. Specifically, we first collected the internal cell representations of ≈ 19 subjects (19.2 ± 5.0)⁶, who experienced status-conversion during our period of interest, and then measured the correlations between the change of the values in the cell states and a transition of the patient’s disease status (0: no conversion and 1: conversion) with point-biserial correlation coefficients. We grouped all subjects depending on the disease transitions

⁶This value represented the mean and standard deviation over the number of subjects in 5-fold cross-validation.

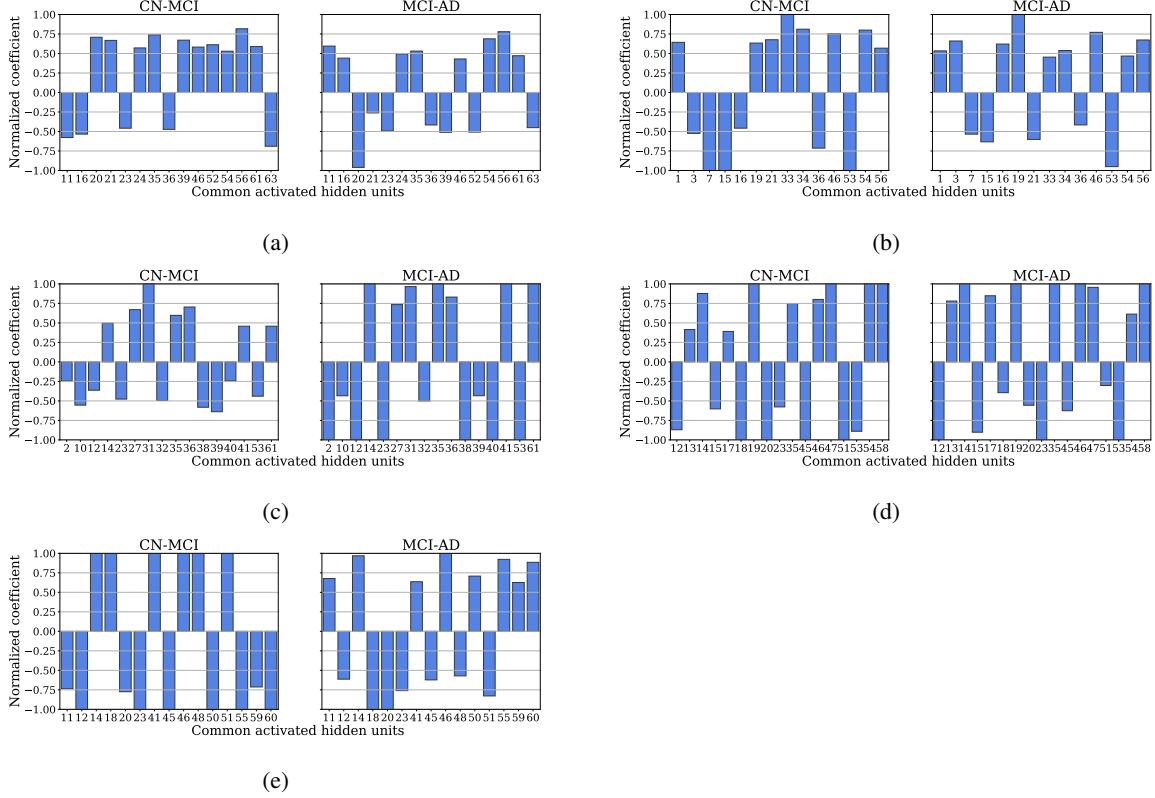


Figure 8: Normalized point biserial correlation coefficients for subjects with conversions, *i.e.*, CN-MCI and MCI-AD, during a period of 10 years from the baseline. Each panel represents the potential cell units for ‘*model biomarkers*,’ whose activations were highly correlated with the conversions.

as follows: (i) ≈ 3 subjects (3.6 ± 2.3) showed transitions from CN to MCI (CN-MCI), (ii) ≈ 13 subjects (13.4 ± 6.0) showed transitions from MCI to AD (MCI-AD), and (iii) ≈ 2 subjects (2.0 ± 1.6) showed transitions through all the statuses of CN, MCI, and AD (CN-MCI-AD). Then, we analyzed the calculated point-biserial correlations for CN-MCI and MCI-AD⁷.

Regarding the variation of conversion time among subjects per group, we normalized the point-biserial correlation coefficients with the standard deviation of the coefficients in each group. Then, we sorted the normalized coefficients to identify the significant cell states related to the transitions, as presented in Fig. E.3. From the sorted cells, we focused on cell units with the top 25% most extreme coefficients per group. Of the selected cell units, the common ≈ 15 cell units (15.4 ± 1.1) in both groups are presented in Fig. 8, where the subfigures correspond to one fold of our five-fold cross-validation experiments. As these cell states showed high correlations either positively or negatively, we believe that those cell units could be potentially used as ‘*model biomarkers*’ with respect to the clinical status conversion. Interestingly, across the five-fold experiments, a similar number (14~17) of cell units showed high correlation with the clinical status change.

⁷We excluded the CN-MCI-AD group for simplicity in interpretation.

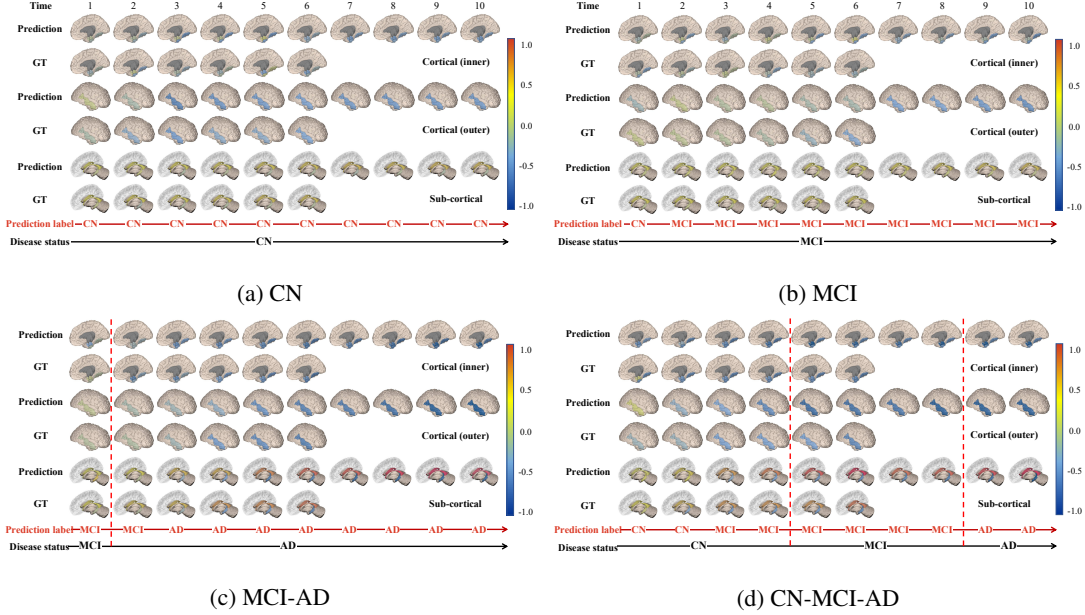


Figure 9: Examples of individual trajectories of MRI biomarkers are the amount of change over time. The color-coded values indicate the normalized relative changes from the respective regions' values at baseline. (GT: ground truth)

From this observation, we infer the robustness or generalizability of our method over different training sets.

5.6. Individual MRI Biomarker Value Changes over Time

In regard to the relationship between the MRI biomarker values and the clinical statuses over time, we visualized the trajectories of the amount of MRI biomarker change and the corresponding clinical status in Fig. 9. We computed the relative changes in the prediction (p) and the ground truth (g) from the respective regions' values to the baseline as follows:

$$r_{g,t}^{(i)} = \frac{y_t^{(i)} - y_0^{(i)}}{y_0^{(i)}}, \quad r_{p,t}^{(i)} = \frac{\hat{y}_t^{(i)} - y_0^{(i)}}{y_0^{(i)}}$$

where i and t denote the indices of MRI biomarkers and time points, respectively. Those relative changes were then normalized with the minimum and maximum values such that the resulting values were in the range of -1 to 1, in which the positive and negative values denote increasing and decreasing, respectively. As a result, in comparisons between the predictions and the ground truths, they showed very similar values over time and across cases. This again demonstrates that our proposed method was good at forecasting the longitudinal MRI biomarkers. Second, unlike the two examples of Fig. 9a and Fig. 9b, which presents stable or slowly deteriorating status over the period, when involving the progression to other statuses in the AD spectrum (Fig. 9c and Fig. 9d), there were relatively rapid changes in values, *i.e.*, enlarged ventricles and shrunken other (sub)cortical regions.

6. Conclusion

Progressive neurodegenerative AD is of great concern around the world due to its clinical, social, and economic impacts. As there is no treatment or medicine to cure or reverse the progression of AD itself, many researchers in various fields have been devoting their efforts to early diagnosis or prognosis in diverse ways. In particular, the use of neuroimaging data is one of the main areas of study, as it provides quantitative and qualitative measurements on which we can build computational models to predict the risk of AD progression.

Of various strategies for accurate AD diagnosis or prognosis, recent studies on longitudinal datasets validated the significance of using historical observations. In that regard, we formulated the problem of AD progression prognosis, *i.e.*, the tasks of MRI biomarker forecasting and clinical status prediction over multiple time points, by means of the disease progression modeling. From a methodological standpoint, we proposed a deep recurrent neural network that is jointly and systematically capable of imputing missing observations, encoding historical inputs into hidden state vector representations, and predicting future MRI biomarker values and the respective clinical status. We have performed exhaustive experiments and analyses by comparing with other comparative methods in the literature. First, our proposed method was superior to those competing methods in various quantitative metrics. Second, our method resulted in more stable (low-bias and low-variance) outputs in MRI biomarker forecasting and more reasonable clinical status prediction by reflecting the characteristics of irreversible AD (*i.e.*, no status-reverse prediction was made over time). Lastly, we observed that some internal state vector representations, *i.e.*, the cell states in our LSTM, showed high correlation with the clinical state-conversion, implying the potential use of those as '*model biomarkers*' in predicting clinical status conversion in the near future.

As we considered only the six MRI biomarkers in this work, our forthcoming research direction will be to accommodate the MRI biomarkers of the whole brain and to integrate functional and/or genotypic information in multi-modal learning. Further, in order to get new insights about the AD progression, it is also important to adopt interpretable and explainable mechanisms in the model.

Acknowledgement

We would like to thank Eunjin Jeon for useful discussions and helpful comments. This work was supported by Institute of Information & communications Technology Planning & Evaluation (IITP) grant funded by the Korea government(MSIT) (No. 2019-0-00079, Department of Artificial Intelligence(Korea University)) and the National Research Foundation of Korea (NRF) grant funded by the Korea government (MEST) (No. NRF-2019R1A2C1006543).

References

References

Aghili, M., Tabarestani, S., Adjouadi, M., Adeli, E., 2018. Predictive Modeling of Longitudinal Data for Alzheimer's Disease Diagnosis using RNNs. International Workshop on Predictive Intelligence In MEdicine , 112–119.

Alzheimer's Association, 2019. 2019 Alzheimer's Disease Facts and Figures. *Alzheimer's & Dementia* 15, 321–387.

Ardekani, B.A., Bermudez, E., Mubeen, A.M., Bachman, A.H., 2017. Prediction of Incipient Alzheimer's Disease Dementia in Patients with Mild Cognitive Impairment. *Journal of Alzheimer's Disease* 55, 269–281.

Bilgel, M., Jedyak, B., Wong, D.F., Resnick, S.M., Prince, J.L., 2015. Temporal Trajectory and Progression Score Estimation from Voxelwise Longitudinal Imaging Measures: Application to Amyloid Imaging, in: International Conference on Information Processing in Medical Imaging, Springer. pp. 424–436.

Bilgel, M., Prince, J.L., Wong, D.F., Resnick, S.M., Jedyak, B.M., 2016. A Multivariate Nonlinear Mixed Effects Model for Longitudinal Image Analysis: Application to Amyloid Imaging. *NeuroImage* 134, 658–670.

Braak, H., Braak, E., 1996. Development of Alzheimer-related Neurofibrillary Changes in the Neocortex Inversely Recapitulates Cortical Myelogenesis. *Acta Neuropathologica* 92, 197–201.

Brookmeyer, R., Johnson, E., Ziegler-Graham, K., Arrighi, H.M., 2007. Forecasting the Global Burden of Alzheimer's Disease. *Alzheimer's & Dementia* 3, 186–191.

Cao, W., Wang, D., Li, J., Zhou, H., Li, L., Li, Y., 2018. BRITS: Bidirectional Recurrent Imputation for Time Series, in: Advances in Neural Information Processing Systems, pp. 6775–6785.

Che, Z., Purushotham, S., Cho, K., Sontag, D., Liu, Y., 2018. Recurrent Neural Networks for Multivariate Time Series with Missing Values. *Scientific Reports* 8, 6085.

Cheng, D., Liu, M., Fu, J., Wang, Y., 2017. Classification of MR Brain Images by Combination of Multi-CNNs for AD Diagnosis 10420, 1042042.

Davis, Wright, 1977. A New Method for Measuring Cranial Cavity Volume and Its Application to the Assessment of Cerebral Atrophy at Autopsy. *Neuropathology and Applied Neurobiology* 3, 341–358.

Fiot, J.B., Raguet, H., Risser, L., Cohen, L.D., Fripp, J., Vialard, F.X., Alzheimer's Disease Neuroimaging Initiative and others, 2014. Longitudinal Deformation Models, Spatial Regularizations and Learning Strategies to Quantify Alzheimer's Disease Progression. *NeuroImage: Clinical* 4, 718–729.

Gaugler, J., James, B., Johnson, T., Marin, A., Weuve, J., 2019. 2019 Alzheimer's Disease Facts and Figures. *Alzheimers & Dementia* 15, 321–387.

Gers, F.A., Schmidhuber, E., 2001. LSTM Recurrent Networks Learn Simple Context-Free and Context-Sensitive Languages. *IEEE Transactions on Neural Networks* 12, 1333–1340.

Gers, F.A., Schmidhuber, J., 2000. Recurrent Nets that Time and Count, in: Proceedings of the IEEE-INNS-ENNS International Joint Conference on Neural Networks, pp. 189–194 vol.3.

Gers, F.A., Schmidhuber, J., Cummins, F., 1999. Learning to Forget: Continual Prediction with LSTM .

Ghazi, M.M., Nielsen, M., Pai, A., Cardoso, M.J., Modat, M., Ourselin, S., Sørensen, L., Alzheimer's Disease Neuroimaging Initiative and others, 2019. Training Recurrent Neural Networks Robust to Incomplete Data: Application to Alzheimer's Disease Progression Modeling. *Medical Image Analysis* 53, 39–46.

Gray, K.R., Wolz, R., Heckemann, R.A., Aljabar, P., Hammers, A., Rueckert, D., Alzheimer's Disease Neuroimaging Initiative and others, 2012. Multi-Region Analysis of Longitudinal FDG-PET for the Classification of Alzheimer's Disease. *NeuroImage* 60, 221–229.

Guerrero, R., Schmidt-Richberg, A., Ledig, C., Tong, T., Wolz, R., Rueckert, D., Alzheimer's Disease Neuroimaging Initiative and others, 2016. Instantiated Mixed Effects Modeling of Alzheimer's Disease Markers. *NeuroImage* 142, 113–125.

Hand, D.J., Till, R.J., 2001. A Simple Generalisation of the Area Under the ROC Curve for Multiple Class Classification Problems. *Machine Learning* 45, 171–186.

Hochreiter, S., Schmidhuber, J., 1997. Long Short-Term Memory. *Neural Computation* 9, 1735–1780.

Ibrahim, J.G., Molenberghs, G., 2009. Missing Data Methods in Longitudinal Studies: a Review. *Test* 18, 1–43.

Jung, W., Mulyadi, A.W., Suk, H.I., 2019. Unified Modeling of Imputation, Forecasting, and Prediction for AD Progression, in: International Conference on Medical Image Computing and Computer-Assisted Intervention, Springer. pp. 168–176.

Kingma, D.P., Ba, J., 2014. ADAM: A Method for Stochastic Optimization. *arXiv preprint arXiv:1412.6980* .

Lee, G., Nho, K., Kang, B., Sohn, K.A., Kim, D., 2019. Predicting Alzheimer's Disease Progression using Multi-Modal Deep Learning Approach. *Scientific Reports* 9, 1–12.

Lin, T.Y., Goyal, P., Girshick, R., He, K., Dollár, P., 2017. Focal Loss for Dense Object Detection , 2980–2988.

Lipton, Z.C., Kale, D.C., Wetzel, R., 2016. Modeling Missing Data in Clinical Time Series with RNNs. *Machine Learning for Healthcare* 56.

Liu, M., Cheng, D., Yan, W., Alzheimer's Disease Neuroimaging Initiative and others, 2018a. Classification of Alzheimer's Disease by Combination of Convolutional and Recurrent Neural Networks using FDG-PET Images. *Frontiers in Neuroinformatics* 12, 35.

Liu, M., Zhang, J., Adeli, E., Shen, D., 2018b. Joint Classification and Regression via Deep Multi-Task Multi-Channel Learning for Alzheimer's Disease Diagnosis. *IEEE Transactions on Biomedical Engineering* 66, 1195–1206.

Lorenzi, M., Filippone, M., Frisoni, G.B., Alexander, D.C., Ourselin, S., Alzheimer's Disease Neuroimaging Initiative and others, 2019. Probabilistic Disease Progression Modeling to Characterize Diagnostic Uncertainty: Application to Staging and Prediction in Alzheimer's Disease. *NeuroImage* 190, 56–68.

Marinescu, R., Eshaghi, A., Alexander, D., Golland, P., 2019. BrainPainter: A Software for the Visualisation of Brain Structures, Biomarkers and Associated Pathological Processes. *arXiv preprint arXiv:1905.08627*

.

Marinescu, R.V., Oxtoby, N.P., Young, A.L., Bron, E.E., Toga, A.W., Weiner, M.W., Barkhof, F., Fox, N.C., Klein, S., Alexander, D.C., et al., 2018. TADPOLE Challenge: Prediction of Longitudinal Evolution in Alzheimer's Disease. *arXiv preprint arXiv:1805.03909* .

McNemar, Q., 1947. Note on the Sampling Error of the Difference between Correlated Proportions or Percentages. *Psychometrika* 12, 153–157.

Miller Jr, R.G., 2011. *Survival Analysis*. volume 66. John Wiley & Sons.

Mills, K.L., Tamnes, C.K., 2014. Methods and Considerations for Longitudinal Structural Brain Imaging Analysis across Development. *Developmental Cognitive Neuroscience* 9, 172–190.

Misra, C., Fan, Y., Davatzikos, C., 2009. Baseline and Longitudinal Patterns of Brain Atrophy in MCI Patients, and Their Use in Prediction of Short-Term Conversion to AD: Results from ADNI. *NeuroImage* 44, 1415–1422.

Morris, J., Storandt, M., McKeel, D., Rubin, E., Price, J., Grant, E., Berg, L., 1996. Cerebral Amyloid Deposition and Diffuse Plaques in “Normal” Aging: Evidence for Presymptomatic and Very Mild Alzheimer's Disease. *Neurology* 46, 707–719.

Nestor, S.M., Rupsingh, R., Borrie, M., Smith, M., Accomazzi, V., Wells, J.L., Fogarty, J., Bartha, R., Alzheimer's Disease Neuroimaging Initiative, 2008. Ventricular Enlargement as a Possible Measure of Alzheimer's Disease Progression Validated Using The Alzheimer's Disease Neuroimaging Initiative Database. *Brain* 131, 2443–2454.

Oulhaj, A., Wilcock, G.K., Smith, A.D., de Jager, C.A., 2009. Predicting the Time of Conversion to MCI in the Elderly: Role of Verbal Expression and Learning. *Neurology* 73, 1436–1442.

Oxtoby, N.P., Alexander, D.C., 2017. Imaging Plus X: Multimodal Models of Neurodegenerative Disease. *Current Opinion in Neurology* 30, 371.

Patterson, C., 2018. World Alzheimer Report 2018: The State Of The Art Of Dementia Research: New Frontiers. Alzheimer's Disease International (ADI): London, UK .

Petersen, R.C., Aisen, P., Beckett, L.A., Donohue, M., Gamst, A., Harvey, D.J., Jack, C., Jagust, W., Shaw, L., Toga, A., et al., 2010. Alzheimer's Disease Neuroimaging Initiative (ADNI): Clinical Characterization. *Neurology* 74, 201–209.

Peterson, K., Rudovic, O., Guerrero, R., Picard, R.W., 2017. Personalized Gaussian Processes for Future Prediction of Alzheimer's Disease Progression. *arXiv preprint arXiv:1712.00181* .

Shi, B., Chen, Y., Zhang, P., Smith, C.D., Liu, J., Alzheimer's Disease Neuroimaging Initiative and others, 2017. Nonlinear Feature Transformation and Deep Fusion for Alzheimer's Disease Staging Analysis. *Pattern Recognition* 63, 487–498.

Suk, H.I., Lee, S.W., Shen, D., Alzheimer's Disease Neuroimaging Initiative and others, 2016. Deep Sparse Multi-Task Learning for Feature Selection in Alzheimer's Disease Diagnosis. *Brain Structure and Function* 221, 2569–2587.

Suk, H.I., Lee, S.W., Shen, D., Initiative, A.D.N., et al., 2014. Hierarchical Feature Representation and Multimodal Fusion with Deep Learning for AD/MCI Diagnosis. *NeuroImage* 101, 569–582.

Suk, H.I., Shen, D., 2013. Deep Learning-based Feature Representation for AD/MCI Classification, in: International Conference on Medical Image Computing and Computer-Assisted Intervention, Springer. pp. 583–590.

Sukkar, R., Katz, E., Zhang, Y., Raunig, D., Wyman, B.T., 2012. Disease Progression Modeling using Hidden Markov Models, in: 2012 Annual International Conference of the IEEE Engineering in Medicine and Biology Society, IEEE. pp. 2845–2848.

Thung, K.H., Yap, P.T., Adeli, E., Lee, S.W., Shen, D., Alzheimer's Disease Neuroimaging Initiative and others, 2018. Conversion and Time-to-Conversion Predictions of Mild Cognitive Impairment using Low-rank Affinity Pursuit Denoising and Matrix Completion. *Medical Image Analysis* 45, 68–82.

Wang, T., Qiu, R.G., Yu, M., 2018. Predictive Modeling of the Progression of Alzheimer's Disease with Recurrent Neural Networks. *Scientific Reports* 8, 9161.

Wei, R., Li, C., Fogelson, N., Li, L., 2016. Prediction of Conversion from Mild Cognitive Impairment to Alzheimer's Disease using MRI and Structural Network Features. *Frontiers in Aging Neuroscience* 8, 76.

Wilcoxon, F., 1992. Individual Comparisons by Ranking Methods. *Breakthroughs in Statistics* , 196–202.

Yoon, J., Zame, W.R., Van der Schaar, M., 2018. Estimating Missing Data in Temporal Data Streams Using Multi-Directional Recurrent Neural Networks. *IEEE Transactions on Biomedical Engineering* 66, 1477–1490.

Zhang, D., Shen, D., Initiative, A.D.N., et al., 2012. Predicting Future Clinical Changes of MCI Patients Using Longitudinal and Multimodal Biomarkers. *PLoS One* 7.

Zhang, D., Wang, Y., Zhou, L., Yuan, H., Shen, D., Alzheimer's Disease Neuroimaging Initiative and others, 2011. Multimodal Classification of Alzheimer's Disease and Mild Cognitive Impairment. *NeuroImage* 55, 856–867.

Appendix A. Summary of the TADPOLE dataset

Table A.1: Demographic information of subjects in the TADPOLE dataset. Values are reported as a mean \pm standard deviation. Note that the number of subjects is measured at the baseline time point and includes missing observation values and clinical statuses during the subject's visits.

Clinical Status	# of subjects		# of visits		Age (mean \pm std.)	
	Male	Female	Male	Female	Male	Female
Cognitively Normal (CN)	253	270	2, 126	2, 084	75.10 \pm 5.64	74.42 \pm 5.38
Mild Cognitive Impairment (MCI)	515	357	4, 207	2, 756	73.71 \pm 7.11	71.80 \pm 7.85
Alzheimer's Disease (AD)	189	153	884	684	75.56 \pm 7.11	74.52 \pm 7.81
All	1, 737		12, 741		73.81 \pm 6.97	

Appendix B. Anatomical regions of the 6 MRI Biomarkers

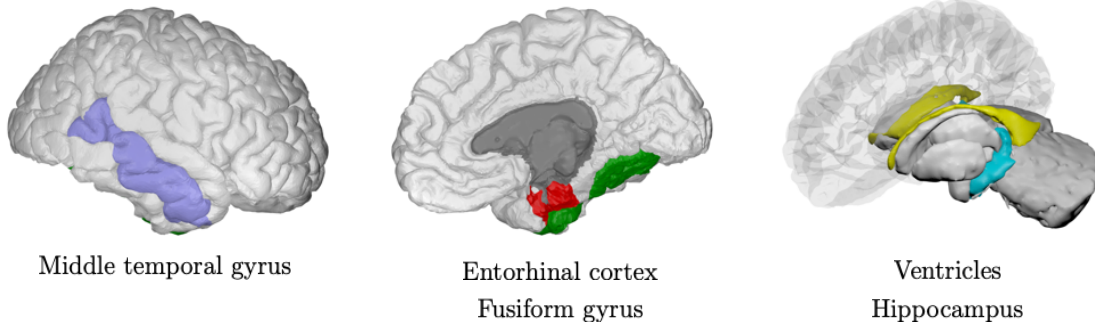


Figure B.1: Visualization of six MRI volumetric biomarkers that are used in our experiments. This figure was generated by the Brain-Painter (Marinescu et al., 2019).

Appendix C. Statistics of the Demographic and Clinical Scores

Table C.2: Statistical information on a demographic and clinical score for each group every year. Scores on the CDR-SOB, ADAS-cog11, and ADAS-cog13 were higher at severe levels of cognitive dysfunction. Conversely, scores on the MMSE were lower at serious levels of cognitive dysfunction.

Year	Groups	Number (Gender)	Age	MMSE	ADAS-cog11	ADAS-cog13	CDR-SOB
Baseline	CN	271 (M/F: 137/134)	74.7±5.5	29.1±1.1	5.9±2.8	9.1±4.2	0.0±0.1
	MCI	483 (M/F: 289/194)	72.1±7.4	27.7±1.8	9.8±4.4	15.8±6.6	1.5±0.9
	AD	19 (M/F: 9/10)	74.8±6.6	22.7±1.9	20.1±5.8	30.9±7.1	4.0±1.4
1	CN	282 (M/F: 139/143)	74.1±5.9	29.1±1.2	5.2±2.8	8.1±4.3	0.1±0.3
	MCI	413 (M/F: 249/164)	72.5±7.4	27.7±2.1	9.4±4.9	15.0±7.2	1.6±1.2
	AD	73 (M/F: 44/29)	72.5±7.0	22.8±4.0	18.7±7.0	29.0±8.6	4.3±1.8
2	CN	275 (M/F: 143/132)	74.1±5.9	29.2±1.1	5.3±3.1	8.4±4.6	0.1±0.4
	MCI	336 (M/F: 194/142)	72.4±7.5	27.8±2.0	9.1±4.6	14.7±7.1	1.5±1.0
	AD	136 (M/F: 84/52)	72.9±7.0	22.3±4.3	19.7±8.6	29.6±9.7	5.3±2.3
3	CN	191 (M/F: 95/96)	73.8±6.1	29.1±1.2	5.0±2.5	8.1±4.0	0.2±0.4
	MCI	296 (M/F: 177/119)	72.3±7.5	27.8±2.1	9.0±4.9	14.4±7.3	1.5±1.2
	AD	153 (M/F: 87/66)	73.2±6.8	21.2±5.4	22.1±10.6	31.8±11.1	6.2±3.2
4	CN	187 (M/F: 93/94)	73.2±6.3	29.1±1.2	5.6±2.9	8.6±4.5	0.1±0.4
	MCI	202 (M/F: 123/79)	72.0±7.2	28.0±1.9	8.3±4.0	13.5±6.2	1.4±1.1
	AD	110 (M/F: 65/45)	72.1±6.8	20.6±5.3	22.9±11.7	33.6±13.6	6.5±3.1
5	CN	93 (M/F: 45/48)	74.1±5.9	29.2±1.2	5.6±3.3	8.8±4.7	0.1±0.3
	MCI	111 (M/F: 70/41)	72.0±7.0	27.5±2.1	8.9±4.1	14.4±6.6	1.6±1.2
	AD	61 (M/F: 34/27)	72.1±6.7	20.1±5.8	26.2±13.2	37.5±15.6	7.2±3.4
6	CN	83 (M/F: 42/41)	74.5±4.8	28.9±1.5	5.7±2.9	9.0±4.4	0.2±0.3
	MCI	61 (M/F: 42/19)	73.9±6.8	27.7±2.1	9.6±4.9	15.3±7.2	1.6±1.5
	AD	49 (M/F: 28/21)	73.1±6.7	18.5±6.2	27.4±14.7	38.9±16.6	8.1±3.8
7	CN	61 (M/F: 32/29)	74.8±4.2	29.1±1.2	5.0±2.8	8.2±4.0	0.2±0.4
	MCI	59 (M/F: 37/22)	74.4±6.2	27.8±1.9	9.6±4.3	15.6±6.9	1.4±1.0
	AD	34 (M/F: 18/16)	72.1±6.4	18.7±5.6	27.5±12.1	39.5±13.5	8.7±3.6
8	CN	43 (M/F: 23/20)	75.3±4.6	28.8±1.3	5.7±2.8	9.4±4.2	0.2±0.4
	MCI	40 (M/F: 26/14)	74.1±6.4	27.6±2.3	10.4±4.9	16.5±6.9	1.5±1.1
	AD	30 (M/F: 18/12)	73.5±6.9	19.2±6.4	25.6±12.1	37.3±14.5	7.3±3.7
9	CN	26 (M/F: 14/12)	73.8±3.5	29.2±1.3	5.3±2.4	8.1±3.7	0.1±0.3
	MCI	29 (M/F: 17/12)	73.3±5.9	27.9±2.4	9.3±3.8	14.9±5.9	1.3±1.2
	AD	27 (M/F: 15/12)	74.7±5.9	19.4±4.8	22.6±8.0	33.9±10.0	6.8±4.3
10	CN	20 (M/F: 10/10)	74.9±4.8	28.9±1.0	5.5±2.9	9.6±4.5	0.1±0.2
	MCI	20 (M/F: 14/6)	76.0±5.8	27.2±2.1	11.2±5.3	17.6±7.9	1.8±1.5
	AD	14 (M/F: 7/7)	73.5±4.9	21.4±6.1	23.1±11.6	33.9±14.0	6.9±2.7

* Age, MMSE, CDR-SB, ADAS-cog11, and ADAS-cog13 are listed as (Mean ± Standard deviation).

* Abbreviation: AD, Alzheimer's disease; ADAS-cog, Alzheimer's Disease Assessment Scale-cognitive subscale; CDR-SOB, Clinical Dementia Rating scale-Sum of the Boxes; CN, Cognitively Normal; F, Female; M, Male; MCI, Mild Cognitive Impairment; MMSE, Mini-Mental State Examination.

Appendix D. Performance across Time

We took the average of the metrics, *i.e.*, mAUC, precision, and recall, from all time sequences, with a result of $\text{mAUC} = 0.7718$, precision = 0.4821, and recall = 0.5361.

Table D.3: Longitudinal regression results for each year in each of the specific volumes for the brain. We observed that the data imbalance was caused over time but the performance did not change significantly. Additionally, the value of MAE decreased and the accuracy of classification increased over time.

Year	1	2	3	4	5	6	7	8	9	10
# of subjects										
CN	141	134	91	92	49	42	29	23	14	10
MCI	203	167	146	103	56	26	27	17	10	6
AD	41	76	87	58	26	25	16	14	16	6
MRI Biomarker Regression (MAE)										
Ventricles	2.616	2.533	2.549	2.102	1.787	1.969	1.884	2.512	2.557	1.643
Hippocampus	0.182	0.168	0.163	0.166	0.175	0.191	0.181	0.208	0.221	0.081
Whole Brain	11.905	11.379	10.436	14.339	16.579	17.909	17.073	18.828	7.559	10.410
Entorhinal Cortex	0.205	0.196	0.158	0.267	0.233	0.204	0.271	0.143	0.390	0.036
Fusiform Gyrus	0.438	0.452	0.353	0.561	0.558	0.590	0.545	0.426	0.558	0.600
Middle Temporal Gyrus	0.486	0.498	0.551	0.608	0.610	0.691	0.815	0.368	0.401	0.066
AD vs. MCI vs. CN										
mAUC	0.716	0.756	0.794	0.778	0.786	0.760	0.786	0.757	0.761	0.824
Precision	0.553	0.492	0.572	0.471	0.547	0.286	0.529	0.438	0.333	0.600
Recall	0.695	0.701	0.678	0.709	0.625	0.308	0.333	0.412	0.400	0.500

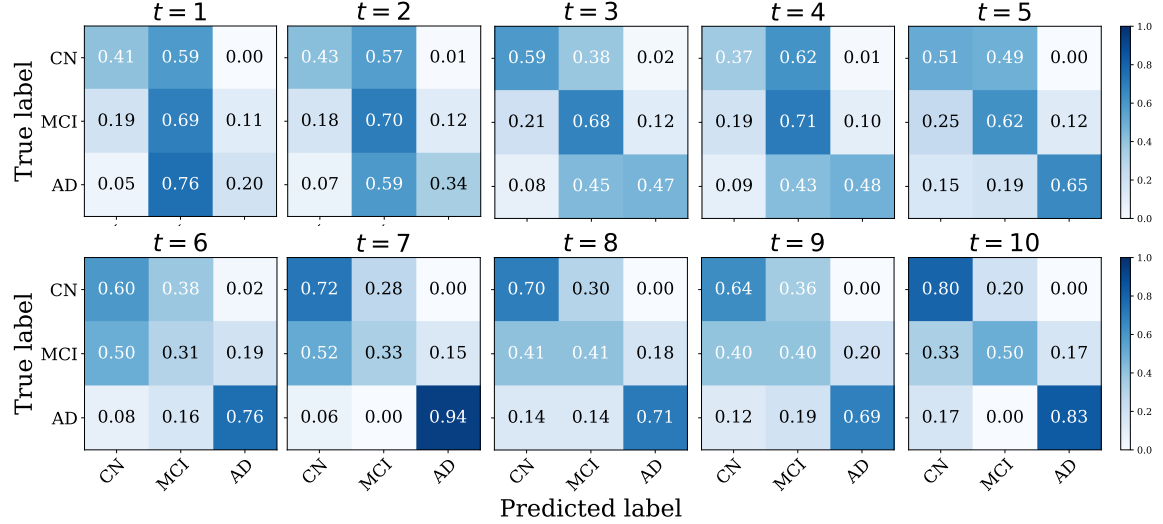


Figure D.2: Yearly computed multi-class classification confusion matrices with normalization using our proposed method. The diagonal elements are the number of points where the predicted labels were the same as the real labels, excluding missing labels, whereas the non-diagonal elements were misclassified by our proposed method. The higher the diagonal value and the darker the shade of blue, the more accurate is the diagnosis of the clinical status.

Appendix E. Interpreting Cell States

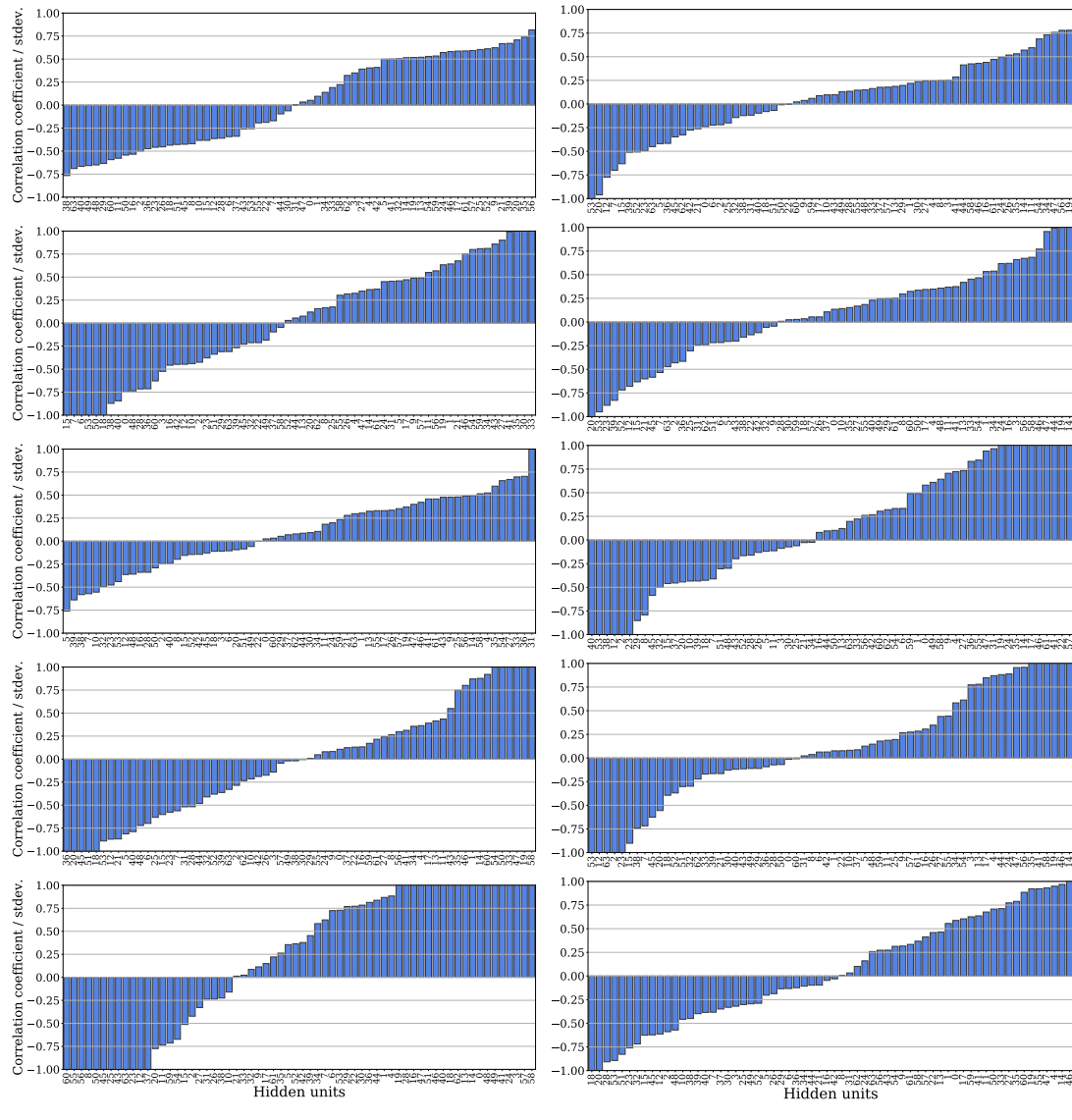


Figure E.3: Normalized point biserial correlation coefficients for subjects with conversion from CN to MCI (left) and from MCI to AD (right) during a period of 10 years from the baseline.